ACS OMEGA

http://pubs.acs.org/journal/acsodf

Article

# Quantitative Correlation of Droplets on Galvanic-Coupled Arrays with Response Current by Image Processing

Moataz Mekawy, Eiji Terada, Shinji Inoue, Yukihiro Sakamoto, and Jin Kawakita*

Cite This: *ACS Omega* 2021, 6, 30818−30825

Read Online

ACCESS | Metrics & More | Article Recommendations

**ABSTRACT:** Evaluating the presence of a slight amount of water plays a crucial role in practical applications such as the advanced detection of dew condensation and the microdetermination of perspiration and transpiration. For this purpose, we have developed a configuration for the moisture sensor that consists of a microgalvanic cell composed of narrow metal arrays. It is inferred that the output response current arising from this sensor should depend on the geometric parameters (e.g., number, area, volume, etc.) of water droplets attaching on the sensor surface. In this study, the output current was recorded, while the microscopic images of the sensor surface were captured. The droplets on the sensor surface were analyzed manually and by computational image processing with deep learning and ImageJ. The deep learning technique shortened the processing time to 1/1000 of the manual one and was able to match 90−100% of the manual count. The results revealed that the response current increased with the total projected area of droplets bridging the galvanic-coupled arrays on the sensor surface. In addition, a straight line with relatively strong positive correlation was obtained between the response current and the total volume of the bridging droplets. These findings suggested that our sensor can be practically used to estimate the presence of a slight amount of water.

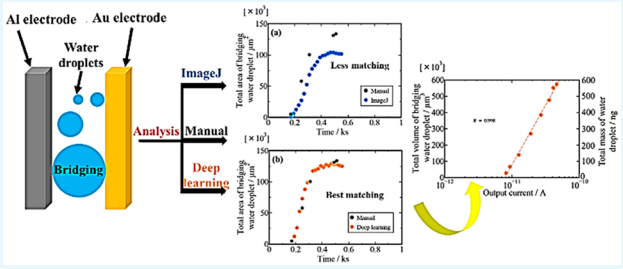


## INTRODUCTION

Evaluating the presence of a slight amount of water is highly required in application fields such as for the advanced detection of dew condensation and microdetermination of perspiration. In particular, real-time monitoring of natural perspiration involves a detailed assessment of body's entire humidity addressing the chemistry and physiology of the body. However, recently proposed techniques could not provide a direct contact detection method, and their reusability and repeatability are still not clear.[1−4] In addition, the early detection of dew condensation is expected to provide precise protection from environmental humidity, avoiding its adverse economic effects.[5,6] Therefore, a system for precise predictive control of humidity/water droplets should be established to control the health conditions and to avoid dew condensation and its worrying consequences in industrial processes such as in pharmaceutical, agricultural, and automobile industries; meteorological monitoring; and other fields.[7−12,14] However, achieving practical systems for the rapid detection of a formed droplet at an early stage with high accuracy remains a challenging task using the ordinary existing technologies. To date, a polymer-based condensation sensor[13] (which cannot distinguish between water droplets and the condensed water vapor) is used despite its low sensitivity. In addition, chilled mirror dew point hygrometers[14] and dew detectors[15] are also used widely despite their limitations such as detection of visible droplets at a considerably large millimeter scale, delayed response and recovery times, narrow humidity detection range (i.e., inability to respond precisely at lower and higher RH), less stability, and above all, inability to quantitatively estimate the detected droplet amount/mass. Therefore, these limitations make these systems inconvenient for practical applications.

In National Institute for Materials Science (NIMS), we developed a microgalvanic cell system termed the moisture sensor that can rapidly and accurately predict small droplets (in a micrometer scale) which are generated during the early dew condensation stage.[16−20] The use of the semiconductor micro-/nanofabrication technology to develop our sensor has enabled us to achieve its facile mass production. Our developed sensor has a Si substrate coated on the $SiO_2$ surface with a repeated comb-like structure of two dissimilar metal electrodes. The intercalated gap between each electrode pair worked as a microgalvanic cell,[16] as shown in Figure 1. In principle, when the water droplet bridges the two electrodes, a rapid response galvanic current is generated in contrast to

**Received:** September 17, 2021
**Accepted:** October 22, 2021
**Published:** November 4, 2021





https://doi.org/10.1021/acsomega.1c05161
*ACS Omega* 2021, 6, 30818−30825

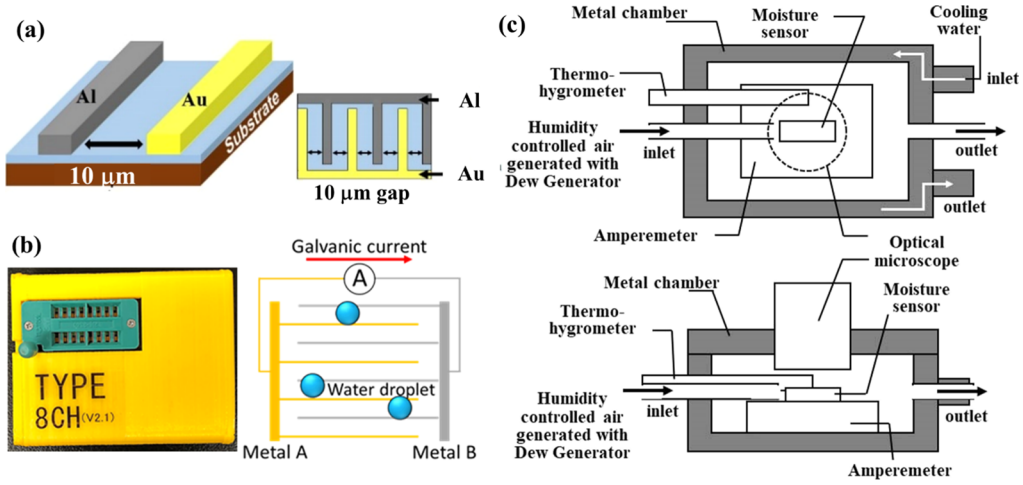


**Figure 1.** Structure and placements of galvanic-coupled arrays on the sensor (a), sensor chip measurement module and schematic illustration of the galvanic arrays and the working principle with water droplets (b), and schematic diagram of simultaneous water droplet generation and sensor surface observation (c).

normal modern hygrometers. This response sheds light on the application feasibility of our developed sensor in, for instance, (1) detection of a slight amount of water and determination of the droplet size spontaneously and accurately.[17] (2) Detection of dew condensation by analyzing the surface nature of the actual target via proper modification of the sensor surface (i.e., changing the wettability of the sensor surface), improving its sensitivity and accuracy.[18] (3) Facile surface modification according to the heat capacity of the actual target object, making it more suitable for various scientific and practical applications.[19] (4) Its output response current showed a linear behavior with the variation in the cooling rate of the sensor surface and the vapor pressure in its vicinity, demonstrating the sensor's ability for advanced detection applications.[20]

Herein, we established a configuration for the moisture sensor that consists of a microgalvanic cell composed of narrow metal arrays associated with an optical microscope. Such a configuration enabled us to simultaneously monitor the adsorbed water droplets on the sensor surface with an optical microscope and measure the stable output response current of the sensor.[16−21] It is worth mentioning that the contact angle between the water droplet and the sensor surface was 33°.[18] Moreover, we did not experience any change in surface roughness or texture during our measurements since we used the same sensor surface throughout this study. From these previous results, it is inferred that the output response current may depend on the geometric parameters (number, area, volume, etc.) of the water droplets adsorbed on the sensor surface, which is still not clear yet. Therefore, in order to correlate the sensor's output response with the geometric parameters of the water droplet quantitatively, it is necessary to measure the output response at different water droplet adsorption states. However, arbitrary control on the adsorption state of water droplets is not possible with the current experimental conditions. Therefore, the number and the total area of water droplets could be effectively evaluated from the corresponding optical images of the sensor surface, and the output response current of the sensor is limited to the water droplets bridging the electrodes. However, analyzing manually and counting the bridging water droplets to extract the relevant water droplets from several images and evaluating their number and projected area require a considerable amount of time and labor. Therefore, computational image processing is highly favorable to reduce the analysis time from hours to seconds.

The purpose of this study is to establish a quantitative correlation between the geometric parameters of water droplets on the sensor surface and the output response current through simultaneous monitoring of water droplets adsorbed on the sensor surface and the measurement of the response current. For such a purpose, the optical images of the sensor surface with adsorbed water droplets were manually analyzed prior to further analysis using computation-based image processing with ImageJ and deep learning.

## EXPERIMENTAL SECTION

**Measurement of Response Current by Droplets with a Moisture Sensor.** The fabrication of our moisture sensor was carried out by Oita Device Technology Co., Ltd, Japan, as described previously.[16−21] In brief, a silicon wafer whose surface was insulated with a silica layer was used as a substrate on which thin arrays made of dissimilar metals were alternately arranged as opposed to comb-like electrodes. The two dissimilar metal electrodes Al and Au were set with 10 $\mu$m gap spacing. Each electrode has a width of 1 $\mu$m and a thickness of 0.15 $\mu$m, as shown in Figure 1a. The repeated number of electrode pairs was 50. Such a combination allows the natural growth of water droplets under controlled humidity on the sensor surface in its effective area (the area needed to generate the galvanic current), which closely matches with the gap spacing. It is expected that the surface nature of the sensor, such as hydrophilicity and hydrophobicity, can remarkably affect the shape and size of water droplets and consequently the galvanic current response.[18,21] The response current from the electrode pairs was collected as an analog signal and converted to digital data by using a module with an electrical circuit, as shown in Figure 1b. The details of the measurement module are also described elsewhere. In this study, the response current was measured at an interval of 200 ms.[18]

**Introduction of Water Droplets on the Sensor's Surface.** The measurement module of the moisture sensor and a thermo-hygrometer (E + E Elektronik/EE23) were installed in a double-walled chamber (Figure 1c). The chamber was cooled by continuously circulating cold water (10 °C)


https://doi.org/10.1021/acsomega.1c05161
ACS Omega 2021, 6, 30818−30825

between the inner and outer walls using a microcirculator. A precision humidity control generator (Micro Equipment Inc., me-40DPRT-2FM-MFC) was used to generate and supply humidity-controlled air in a fixed humidity range of 90% or more to the chamber (near the sensor) at 200 NCCM. Next, the circulating cold water temperature was increased up to 20 °C for 120 s to increase the temperature inside the chamber. Hence, condensation was induced on the sensor surface by keeping its temperature relatively lower than that inside the chamber. After 120 s, the cooling water temperature was returned again to 10 °C and then the water droplets on the sensor surface were evaporated. We used a combination of Al (anode) and Au (cathode) dissimilar electrodes due to the ease of their nanofabrication deposition in addition to the wide potential difference between them. Thus, the oxidation of the Al electrode and the electrochemical oxygen reduction that occurs on the surface of the Au electrode allow the facile detection of the galvanic electric current once the water droplet bridges these two electrodes. Accordingly, the choice of electrode combination is expected to influence the experimental results.

**Observation of the Sensor's Surface.** The sensor surface was simultaneously monitored from the top using a digital camera of an optical microscope (VHX-7000 Series; KEYENCE, Osaka, Japan), as shown in Figure 1c.

**Image Analysis.** Image analysis was performed on the recorded optical images of the sensor's surface, and the total area within the contour of water droplets bridging the electrodes was estimated using three different methods.

**Manual Estimation.** Manual estimation was carried out using the original microscopic images recorded with time as a function of relative humidity and time. The number of water droplets and their area were manually estimated using ImageJ software without any image processing steps.

**Computational Estimation with ImageJ Processing.** Figure 2 shows a typical model of the ImageJ processing

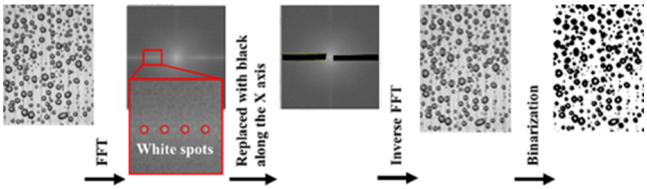


**Figure 2.** ImageJ processing pathway of a microscopic image that includes water droplets straddling the moisture sensor electrodes.

pathway. ImageJ is an open source image analysis software that has been widely used with a proven track record among scientific researchers.[22,23] Its processing in our study started with the selection of microscopic images assuming that the electrodes located on the sensor surface are parallel to the *y*-axis. Thus, the selected image was transformed into its analogous grayscale, followed by the 2-D fast Fourier transform (FFT) operation. Remarkable white spots were recorded at equal distances along the *x*-axis. These spots were mainly due to the electrodes and thus the electrodes' positions were determined. Further processing was carried out using the inverse FFT to eliminate the interference of the electrodes' white spots. Hence, the water droplet spots could be clearly recognized without interference. Using ImageJ automation for pixel adjustment followed by image binarization[24,25] enabled us to determine the position of each droplet by classifying its role in bridging the two electrodes and making a clear distinction of the pure bridging droplets which are responsible for response galvanic current. Thus, the number of droplets along with their correlated areas could be estimated.

**Computational Estimation Using Deep Learning.** Prior to real computational estimation, a training deep learning model was established wherein annotation of bridging water droplets was carried out using selected microscopic images. Accordingly, the number of identified chosen bridging water droplets was adjusted to around 1000. Figure 3 shows a typical model of the deep learning processing pathway.

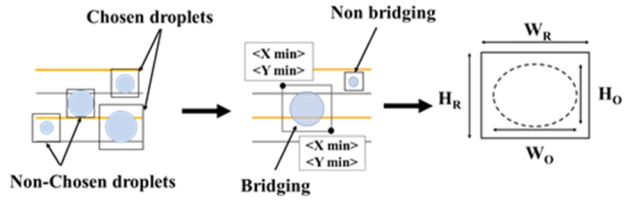


**Figure 3.** Deep learning image processing pathway of water droplets straddling moisture sensor electrodes including the choice of droplets with the area that represents 65% of the rectangular boundary box area followed by bridging classification and final distribution and area estimation. Rectangular height and width: $H_R$ and $W_R$. Oval height and width: $H_O$ and $W_O$.

To execute real-time analysis, a microscopic image was selected followed by inclusion of the identified water droplets (with respect to the training model) within the selected frame of a rectangular boundary box with all probable electrode straddling ways. Based on that, droplets with an area that represents 65% of the outer boundary box area were chosen assuming that the droplet's oval height and width are less than those of the rectangular boundary box (i.e., $H_R W_H = 1.2 W_O H_O$). Therefore, the total area of the oval droplet is about 65% compared to that of the rectangular boundary box. Afterward, further classification of water droplets was carried out to distinguish the bridging droplets which are responsible for the galvanic current response. Position determination was carried out for each distinguished droplet correlating its *x* and *y* coordinates. Finally, the statistical estimation of the number of water droplets and their area was carried out.

## RESULTS AND DISCUSSION

**Relation between the Sensor Output and the Droplet Status.** Figure 4I shows the output current response from the moisture sensor recorded with time during adsorption and desorption of droplets on the sensor surface.

Figure 4II shows the corresponding microscopic images of the sensor surface at different recording times. Before starting the experimental work, the clear surface of the sensor surface is shown in image a. After introducing humid air feed to the chamber that contains the sensor, water droplets are adsorbed onto the sensor surface and bridging between the electrodes took place, leading to the rapid generation of a remarkable output response current (0.15 ks, microscopy image b).

The response current increased when the number of droplets increased on the surface at 0.23 ks, reaching almost a maximum value at 0.39 ks and remained nearly at the same current level up to 0.55 ks. Simultaneously, the corresponding microscopic images (0.39 and 0.55 ks, microscopy images d and e) showed that a large number of water droplets covered a


https://doi.org/10.1021/acsomega.1c05161
ACS Omega 2021, 6, 30818−30825

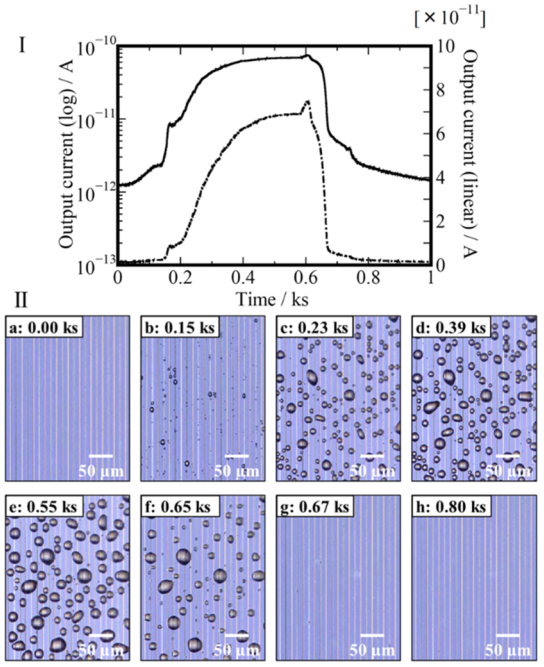


**Figure 4.** Output response current in logarithmic (solid line) and linear (dashed line) scales recorded with time during adsorption and evaporation of droplets on the sensor surface (I). The optical images of the sensor's surface at different times of experiment: (a) 0.00, (b) 0.15, (c) 0.23, (d) 0.39, (e) 0.55, (f) 0.65, (g) 0.67, and (h) 0.80 ks (II).

wider area on the sensor surface than that previously recorded and appeared somehow similar to each other. This indicated that there was no significant change in the apparent water droplet area, with no significant increase or decrease in the observed response current value. Afterward, it was noticed that the current decreased rapidly (0.65 ks, microscopy image f), while fewer water droplets were observed on the sensor surface, indicating that the partial evaporation was taking place. Finally, no response current was recorded, indicating the complete evaporation of the previously adsorbed water droplets (0.80 ks, microscopy image h).

These results indicated that the sensor instantaneously generated a current response due to the adsorption of water droplets that were effectively bridging the electrodes. Hence, the response current depended mainly on the droplets bridging the projected areas and/or the coverage status between electrodes. The projected area is thus defined as the area of the droplet covering the electrodes located on the sensor surface, hereafter denoted generally as area in this paper. Since the output response current decreased to its background value due to the evaporation of bridging water droplets, our analysis in this paper will focus on the bridging process that starts with the generation of response current until reaching its saturation maximum before evaporation. For more clear evidence for the experimental results gained above, we manually estimated the number of water droplets at each time point, as shown in Figure 4II.

It is well known that performing manual image analysis such as a cut-out of some interfering hundred droplets requires a few hours. However, the choice of faster processing image analysis methods is recommended for analyzing within tens of seconds, especially while there are numerous data available. Therefore, computational image processing estimation was carried out using ImageJ and deep learning. Table 1 lists the number of water droplets obtained by manual counting, ImageJ, and deep learning analysis methods at different experimental times.

**Table 1. Number of Water Droplets Bridging Arrays on the Sensor's Surface Counted by Different Methods: Manual Process and Image Analysis by ImageJ and Deep Learning at Certain Times**

| | | image analysis (matching rate % in brackets) | |
|---|---|---|---|
| time/ks | manual process | ImageJ | deep learning |
| 0.15 | 3 | 0 (0) | 3 (100) |
| 0.23 | 331 | 56 (17) | 364 (90) |
| 0.55 | 397 | 228 (57) | 407 (97) |
| 0.65 | 177 | 48 (27) | 184 (96) |

As listed in Table 1, the matching rate of the estimated number of water droplets by deep learning image processing and manual counting was 90−100%, whereas the matching rate was only 0−57% while using ImageJ processing. This is because ImageJ processing could not separate and detect adjacent droplets accurately and regarded a lot of them as one large droplet which consequently gave errors in the estimation of the droplet number. Moreover, it could not recognize droplets when the boundary was not clearly defined. In other words, contrast between their periphery and the background was ambiguous. On the other hand, deep learning processing takes advantage of droplet recognition with such ambiguity and therefore a high matching rate could be achieved.

Figure 5a shows the change in the number of bridging water droplets with time. Experimental results revealed a close matching between the number of water droplets estimated manually and that estimated using deep learning processing, whereas the number of droplets estimated using ImageJ processing showed less matching. Figure 5b shows the histogram distribution between the number of droplets and

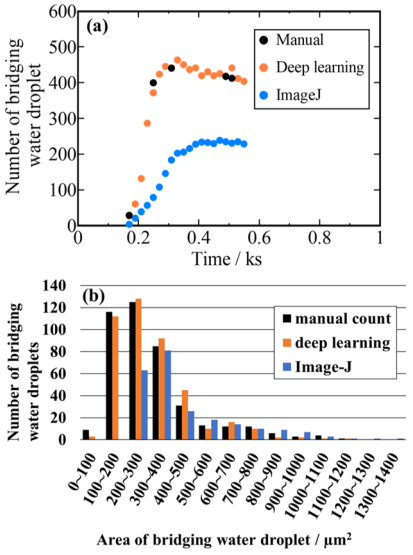


**Figure 5.** Change in the number of bridging water droplets with time (a) and statistical distribution of the bridging water droplets' total area at equilibrium 0.49 ks (b) analyzed by manual count (black), deep learning (orange), and ImageJ (blue).


https://doi.org/10.1021/acsomega.1c05161
ACS Omega 2021, 6, 30818−30825

the total area of bridging water droplets on the sensor surface at 0.49 ks, which was estimated using manual, ImageJ, and deep learning processing methods. The total area is defined as the summation of bridging droplets' areas. These results demonstrated that the estimated total area using deep learning showed a relatively higher degree of distribution agreement with the manual estimation than that estimated using ImageJ which gave wider variances. This is because ImageJ cannot separate and recognize adjacent water droplets as described above and regard them as one large water droplet.

Further confirmation is shown in Figure 6 where the total area of water droplets that was obtained by the three image

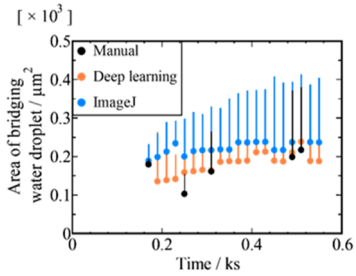


**Figure 6.** Change over time in the total area of water droplet bridging arrays obtained by manual count compared with image processing analyses using ImageJ (blue) and deep learning (orange). Plots and bars represent the mode and the difference between the mode and the value at the third quartile, respectively.

analyses methods is plotted, and the difference up to the value in the third quartile is shown as a variance with respect to time.

Since ImageJ may recognize multiple water droplets as one with a bigger area, it shows slightly larger values at examined time zones, which is more remarkable in the early stage. This is because ImageJ processing analyzes a captured image based on a threshold value of brightness where the Fourier transformation of the output image makes the substrate white and the water droplets black, raising a high possibility of including errors in case any part of the image becomes out of focus. Thus, the output of the excluded water droplet part may not appear as black, and finally the number of water droplets' output becomes lower than the actual though with the estimated larger projected areas.

In contrary, in the case of the image processing with deep learning, it is possible to determine the output number of water droplets with higher accuracy since the water droplets that are out of focus in the case of the ImageJ method are not excluded. Figure 7a,b confirms that the droplets' total area which was estimated using a deep learning processing has a higher matching tendency than those estimated using ImageJ processing once correlated with the total area estimated manually.

Moreover, linear calibration curves confirmed the same results. However, the calibration curve (Figure 8a) showed a large mismatch between the droplets' total area estimated manually and that estimated by ImageJ processing though the expected response galvanic current was higher than that measured experimentally. On the other hand, the calibration curves (Figure 8b) showed better matching with less linearity between the droplets' total area estimated manually and by deep learning processing along with the measured and expected response galvanic current. This could be clearly noticed in the early stages of dew condensation.

These results can be explained by the current-flow model shown in Figure 9. Assuming that the adsorbed water droplet has a hemisphere geometry at an arbitrary time, the effective area which is defined as the area of the water droplet that is effectively intact between electrodes to generate a galvanic current is calculated from the area of the water droplet in the recorded image. Based on the droplet size, we predicted several models with water droplets intact within the electrodes, as shown in Figure 9a. In the first case, when the droplet covers one pair of the electrode zone, the effective area can be expressed simply as one rectangular area ($A_1$), which is smaller than the area of the water droplet. In the second case, when the droplet covers three pairs of electrode zones, the effective area can be expressed by the rectangular area intact in each zone depending on the intact length ($l$). Thus, three areas ($A_1$−$A_3$) can be estimated. In the third case, when the droplet covers five pairs of electrode zones, the effective area in each zone is similarly based on the intact droplet's length ($l$) and thus five areas ($A_1$−$A_5$) can be estimated. Therefore, the effective area estimated in each case is dependent on its corresponding intact length ($l$). Accordingly, the galvanic current which depends on the droplet size will also be varied according to its intact length (with the electrode pair) as well as its effective area.

Taking into account that the galvanic current flows favorably in direction 1, as indicated in Figure 9b, rather than in direction 2, which requires a higher electron energy to overcome the barriers and cross a longer pathway, the effective area ($A_n$) of the droplet that is required to generate the galvanic current can be expressed as follows

$$A_n = (l_n)(g) \quad (1)$$

where $g$ is the gap size between two electrodes (10 $\mu$m) and $l_n$ is the intact length from the electrode to the water droplet.

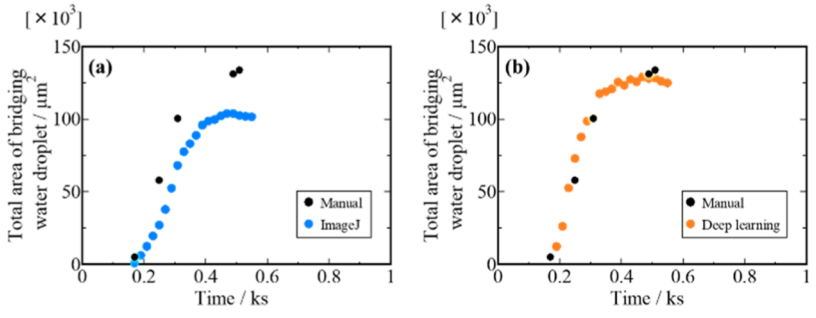


**Figure 7.** Change in the total area of water droplet bridging arrays with time obtained manually and by using image processing ImageJ (a) and deep learning (b).



https://doi.org/10.1021/acsomega.1c05161
ACS Omega 2021, 6, 30818−30825

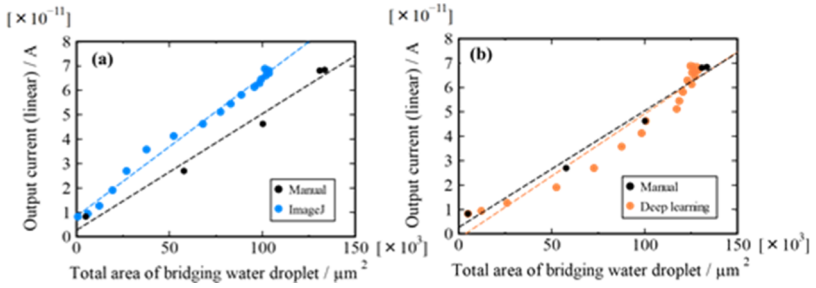


**Figure 8.** Relationship between the recorded response current from the moisture sensor and the total area of water droplet bridging arrays at arbitrary time obtained by image processing analyses of ImageJ (a) and deep learning (b).

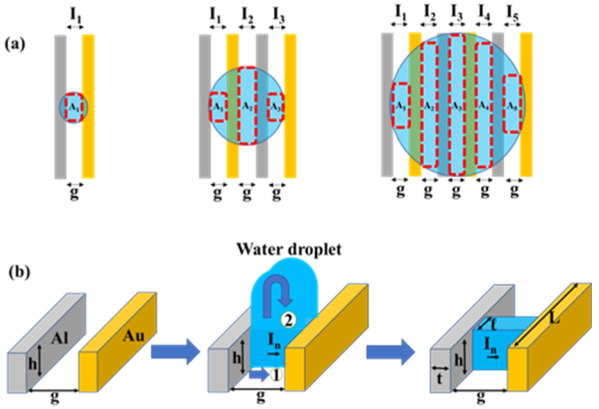


**Figure 9.** Schematic illustration of various total and projected droplets' area based on the size and the intact length of the electrode pair (a). A current-flow estimation model for the intact droplet's effective area assuming that the area has a hemispherical shape and the total effective area has a rectangular shape (b).

Since $g$ is fixed, $l_n$ is the only variable in this equation. Accordingly, the effective area can be precisely estimated.

Rearranging eq 1 to get $l_n$ can lead to

$$l_n = A_n/g \tag{2}$$

Since the resistance can be expressed as

$$R_n = \frac{(\rho)(g)}{(h)(l_n)} \tag{3}$$

where $\rho$ is the resistivity of the electrode material and $R$ is the resistance which can also be expressed using Ohm's law $R_n = E/I_n$, where $E$ is the potential (which is constant in our case) and $I_n$ is the galvanic response current generated by droplet bridging between two electrodes. Therefore

$$I_n = \frac{(E)(h)(A_n)}{(\rho)(g^2)} \tag{4}$$

and $n = 1, 2, 3, \ldots$

Since $E$, $h$, $g$, and $\rho$ are fixed values, the total response current generated from one droplet can be expressed as

$$\sum I_n = \frac{(E)(h)}{(\rho)(g^2)} \sum A_n \tag{5}$$

where $\Sigma A_n$ is the total effective area of the droplet that is intact with the electrode surface and contributes to the generation of the response galvanic current. Therefore, the total effective area is expected to be less than the total droplets' area.

From eq 5, it is evident that the response galvanic current is directly proportional to the total effective area of the water droplet ($I_n \propto A_n$). Moreover, a further increase in the dew condensation leads to an increase in the droplets' area and the effective area as well. Thus, both the measured and expected galvanic current values showed the best matching in linearity due to the total droplets' area contribution. An additional increase in dew condensation results in a saturation region beyond which there is no increase in area. Surprisingly, the galvanic current response showed a remarkable increase even at the saturated area region. This could be ascribed to the existence of continuous charge transfer between the active electrodes' surface and the existing water droplets, which allowed the redox reaction to continue with increasing conductivity, generating higher galvanic current even at a steady droplet's area.

The possible reactions that may occur at the Al anode are

$$4Al \rightarrow 4Al^{3+} + 12e^- \tag{6}$$

$$4Al^{3+} + 3H_2O \rightarrow 2Al_2O_3 + 6H^+ \tag{7}$$

Therefore, the net anode reaction is given by

$$4Al + 6H_2O \rightarrow Al_2O_3 + 12H^+ + 12e^- \tag{8}$$

The reaction that occurs at the Au cathode is written as

$$3O_2 + 6H_2O + 12e^- \rightarrow 12OH^- \tag{9}$$

Therefore, the total reaction can be expressed as follows

$$4Al + 3O_2 + 12H_2O \rightarrow 2Al_2O_3 + 12H^+ + 12OH^- \tag{10}$$

Thus, the contact of Al and Au or any noble metal enables the generation of total response current, expressed as eq 5, to continue even with the formation of $Al_2O_3$. Therefore, our results confirmed that the correlation of the human manual count with the deep learning image processing count showed better matching than that with ImageJ processing. This clarified that deep learning processing shows a high correlation coefficient similar to the human manual count and that the response current correlates with the total effective area of adsorbed water droplets on the electrodes. This indicates that the current value flowing between electrodes is inversely proportional to the resistance, assuming that the potential difference between the electrodes is constant.

Furthermore, assuming that the volume resistivity of water droplets existing between the electrodes is constant, the resistance between the electrodes is inversely proportional to the effective area of the water droplet because the distance between the adjacent electrodes ($g$) is constant. These findings confirmed that deep learning could be more favorable due to


https://doi.org/10.1021/acsomega.1c05161
ACS Omega 2021, 6, 30818−30825

the clear estimation of well-resolved boundaries of water droplets, which is not the case in ImageJ as it cannot differentiate between overlapped droplets and estimates their volume as larger than normal, leading to an unpredicted increase in the expected response current. In addition, this research opens the door for the feasible future applications on the precise estimation of the total volume and/or total mass of the existing droplets as a function of the gained response galvanic current. Figure 10 shows a linear correlation calibration curve of the estimated water droplet volume as a function of the response current.

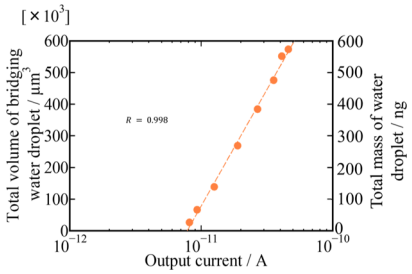


**Figure 10.** Relationship between the estimated volume of the water droplet and the logarithmic response galvanic current.

It is evident from Figure 10 that the volume and consequently the mass of the related dew condensation expressed with water droplets can be estimated once the response current is monitored experimentally. Such an aim was previously studied using different supporting techniques such as quartz crystal microbalance and spray vapor deposition.

Our preliminary findings listed in this study are believed to be the cornerstone for more future comprehensive experimental works studying several other affecting parameters (e.g., surface wettability, texture, stability, etc.) for elucidation of other atmospheric conditions that relate with environmental practical applications.

## CONCLUSIONS

This study demonstrated that the output response current arising from the microgalvanic cell moisture sensor should depend on the geometric parameters of the surface-adsorbed water droplets such as the number, area, and volume estimated by the microscopic observation of the sensor surface and its image analysis. Response current showed a remarkable increase based on the summation of the effective areas, as explained with the current flow model of the droplet. The linear relationship between the sensor's response current and the volume of the surface-adsorbed droplets could be correlated successfully with the quantitative estimation of droplets' mass. Image processing techniques enabled us to decrease the analysis time to around 1/1000. The current study can contribute effectively to practical applications such as micro-determination of dew condensation and perspiration.

## AUTHOR INFORMATION

### Corresponding Author

**Jin Kawakita** − *National Institute for Materials Science, Tsukuba 305-0044, Japan;* orcid.org/0000-0002-4821-4150; Email: KAWAKITA.Jin@nims.go.jp

### Authors

**Moataz Mekawy** − *National Institute for Materials Science, Tsukuba 305-0044, Japan;* orcid.org/0000-0002-3516-7578

**Eiji Terada** − *National Institute for Materials Science, Tsukuba 305-0044, Japan; Chiba Institute of Technology, Chiba 275-0016, Japan*

**Shinji Inoue** − *National Institute for Materials Science, Tsukuba 305-0044, Japan*

**Yukihiro Sakamoto** − *Chiba Institute of Technology, Chiba 275-0016, Japan*

Complete contact information is available at: https://pubs.acs.org/10.1021/acsomega.1c05161

### Author Contributions

M.M., results discussion and model formulation. E.T., experimental setup and data collection. S.I., image processing. E.T. and S.I., manual counting. Y.S., discussion and advice. J.K., conceived the idea, designed the experimental work, and research resources. All authors contributed in writing the manuscript.

### Funding

This research was supported by PRISM (Public/Private R&D Investment Strategic Expansion PrograM), Cabinet Office, Japan, and M-CUBE project in NIMS (National Institute for Materials Science), Japan.

### Notes

The authors declare no competing financial interest.

## REFERENCES

(1) Nyein, H. Y. Y.; Bariya, M.; Tran, B.; Ahn, C. H.; Brown, B. J.; Ji, W.; Davis, N.; Javey, A. A wearable patch for continuous analysis of thermoregulatory sweat at rest. *Nat. Commun.* **2021**, *12*, 1823−1835.

(2) Lin, S.; Wang, B.; Zhao, Y.; Shih, R.; Cheng, X.; Yu, W.; Hojaiji, H.; Lin, H.; Hoffman, C.; Ly, D.; Tan, J.; Chen, Y.; Di Carlo, D.; Milla, C.; Emaminejad, S. Natural Perspiration Sampling and in Situ Electrochemical Analysis with Hydrogel Micropatches for User-Identifiable and Wireless Chemo/Biosensing. *ACS Sens.* **2020**, *5*, 93−102.

(3) Jeong, W.; Song, J.; Bae, J.; Nandanapalli, K. R.; Lee, S. Breathable Nanomesh Humidity Sensor for Real-Time Skin Humidity Monitoring. *ACS Appl. Mater. Interfaces* **2019**, *11*, 44758−44763.

(4) Gao, W.; Emaminejad, S.; Nyein, H. Y. Y.; Challa, S.; Chen, K.; Peck, A.; Fahad, H. M.; Ota, H.; Shiraki, H.; Kiriya, D.; Lien, D-H.; Brooks, G. A.; Davis, R. W.; Javey, A. Fully integrated wearable sensor arrays for multiplexed in situ perspiration analysis. *Nature* **2016**, *529*, 509−514.

(5) Ebbing, D. D.; Wrighton, M. S. *General Chemistry*, 3rd ed.; Houghton Mifflin, 1990.

(6) John, J. W.; Kolb, D. K. *Chemistry for Changing Times*, 9th ed.; Prentice Hall, 2001.

(7) Bridgeman, D.; Corral, J.; Quach, A.; Xian, X.; Forzani, E. Colorimetric humidity sensor based on liquid composite materials for the monitoring of food and pharmaceuticals. *Langmuir* **2014**, *30*, 10785.

(8) Selyanchyn, R.; Wakamatsu, S.; Hayashi, K.; Lee, S.-W. A nano-thin film-based prototype QCM sensor array for monitoring human breath and respiratory patterns. *Sensors* **2015**, *15*, 18834.

(9) Yang, T.; Yu, Y. Z.; Zhu, L. S.; Wu, X.; Wang, X. H.; Zhang, J. Fabrication of silver interdigitated electrodes on polyimide films via surface modification andion-exchange technique and its flexible humidity sensor application. *Sens. Actuators, B* **2015**, *208*, 327.

(10) Su, P.-G.; Chiou, C.-F. Electrical and humidity-sensing properties of reduced graphene oxide thin film fabricated by layer-

by-layer with covalent anchoring on flexible substrate. *Sens. Actuators, B* **2014**, *200*, 9.
(11) Farahani, H.; Wagiran, R.; Hamidon, M. Humidity sensors principle, mechanism, and fabrication technologies: A comprehensive review. *Sensors* **2014**, *14*, 7881.
(12) Pavinatto, F. J.; Paschoal, C. W. A.; Arias, A. C. Printed and flexible biosensor for antioxidants using interdigitated ink-jetted electrodes and gravure-deposited active layer. *Biosens. Bioelectron.* **2015**, *67*, 553.
(13) Chen, Z.; Lu, C. Humidity Sensors: A Review of Materials and Mechanisms. *Sens. Lett.* **2005**, *3*, 274.
(14) Zhu, S.; Lu, Y. F.; Hong, M. H.; Chen, X. Y. Laser ablation of solid substrates in water and ambient air. *J. Appl. Phys.* **2001**, *89*, 2400.
(15) Hornero, G.; Gaitán-Pitre, J. E.; Serrano-Finetti, E.; Casas, O.; Pallas-Areny, R. A novel low-cost smart leaf wetness sensor. *Comput. Electron. Agric.* **2017**, *143*, 286−292.
(16) Kawakita, J.; Chikyow, T. Detection of micro/nano droplet by galvanic current. *ECS Trans.* **2017**, *75*, 51.
(17) Kubota, Y.; Mishra, V. L.; Sakamoto, Y.; Kawakita, J.; Ando, T. Micro/nano galvanic-coupled arrays for early and initial detection and prediction of dew condensation. *Sens. Actuators, A* **2020**, *303*, 111838.
(18) Shrestha, R. G.; Ando, T.; Sakamoto, Y.; Kawakita, J. Enhancement of sensitivity and accuracy of micro/nano water droplets detection using galvanic-coupled arrays. *Sensors* **2019**, *19*, 4500.
(19) Kita, I. "Condensation detection element". WO 2020100778 A1, 2020.
(20) Shrestha, R. G.; Kubota, Y.; Sakamoto, Y.; Kawakita, J. Quick and Sensitive Detection of Water Using Galvanic-Coupled Arrays with a Submicron Gap for the Advanced Prediction of Dew Condensation. *Sensors* **2020**, *20*, 3314.
(21) Shrestha, R. G.; Kawakita, J. Superhydrophilic polymer modified galvanic array moisture sensor chip with stable/improved lifetime towards enhanced dew condensation detection. *Sens. Actuators, A* **2021**, *331*, 113036.
(22) Rasband, W. S. *ImageJ*; United States National Institutes of Health: Bethesda, Maryland, USA, 2012, 1997−2012. http://imagej.nih.gov/ij/.
(23) Schneider, C. A.; Rasband, W. S.; Eliceiri, K. W. NIH Image to ImageJ: 25 years of image analysis. *Nat. Methods* **2012**, *9*, 671−675.
(24) https://imagej.nih.gov/ij/developer/api/ij/gui/Roi.html (accessed December 2020).
(25) https://satoshithermophilus.hatenablog.com/entry/2017/08/08/222531,ImageJautomationin10minutesJythonscript (accessed January 2021).


https://doi.org/10.1021/acsomega.1c05161
*ACS Omega* 2021, 6, 30818−30825